Naval Research Laboratory

Washington, DC 20375-5000

(2)

NRL Report 9336

A New Theory for Image Formation with Quasi-homogeneous Sources and its Application to the Detection and Location of ICBM Launches

W. H. CARTER

Space Systems Technology Department

September 17, 1991

REPORT DOCUMENTATION PAGE

Form Approved
OMB No 0704-0188

1. AGENCY USE ONLY *(Leave blank)*	2. REPORT DATE	3. REPORT TYPE AND DATES COVERED
		September 17, 1991

4. TITLE AND SUBTITLE

A New Theory for Image Formation with Quasi-homogeneous Sources and its Application to the Detection and Location of ICBM Launches

5. FUNDING NUMBERS

6. AUTHOR(S)

W. H. Carter

7. PERFORMING ORGANIZATION NAME(S) AND ADDRESS(ES)

Naval Research Laboratory
Washington, DC 20375-5000

8. PERFORMING ORGANIZATION REPORT NUMBER

NRL Report 9336

9. SPONSORING/MONITORING AGENCY NAME(S) AND ADDRESS(ES)

10. SPONSORING/MONITORING AGENCY REPORT NUMBER

11. SUPPLEMENTARY NOTES

12a. DISTRIBUTION/AVAILABILITY STATEMENT

Approved for public release; distribution unlimited.

12b. DISTRIBUTION CODE

13. ABSTRACT *(Maximum 200 words)*

A new theory describing image formation with three-dimensional, quasi-homogeneous primary sources is developed for application to the problem of detecting and locating ICBM launches. The theory is used to compare telescopes and interferometers that have been suggested for use in "Brilliant Eyes" systems.

14. SUBJECT TERMS

Remote sensing Optical interferometry
Imaging

15. NUMBER OF PAGES

28

16. PRICE CODE

17. SECURITY CLASSIFICATION OF REPORT	18. SECURITY CLASSIFICATION OF THIS PAGE	19. SECURITY CLASSIFICATION OF ABSTRACT	20. LIMITATION OF ABSTRACT
UNCLASSIFIED	UNCLASSIFIED	UNCLASSIFIED	UL

CONTENTS

A NEW THEORY FOR IMAGE FORMATION WITH QUASI-HOMOGENEOUS SOURCES AND ITS APPLICATION TO THE DETECTION AND LOCATION OF ICBM LAUNCHES

1. INTRODUCTION

The detection of the launch of an ICBM-type missile by a hostile country toward the United States is of serious interest to the "Brilliant Eyes" program. The most easily detected signature from the launch of the missile appears to be the thermal radiation from the exhaust of the booster rocket. This radiation can be expected to be bright and easily detected against the sky provided that the radiation is not concealed by clouds, solar background, or other such phenomena.

The radiation from an ICBM booster rocket can be analyzed by the use of the quasi-homogeneous source model developed by Carter and Wolf [1]. In this report, such an analysis is done for the first time to compare the various methods that have been suggested for detecting an ICBM launch and locating its position. In Section 2, a theory describing the basic imaging problem is developed by using the methods of optical coherence theory with the quasi-homogeneous source model. In Section 3, a generalized imaging system, which can be used to describe most all of the imaging systems considered for the ICBM launch detection problem, is described by use of this theory. Section 4 discusses the limitations of small imaging system apertures on the resulting image and modifies the theory to account for this effect. Section 5 specializes the generalized imaging system to study the imaging properties of interferometers (similar to the radio interferometers used for radio astronomy). And Section 6 describes how the generalized imaging system studies the imaging properties of the more conventional telescope.

This theory shows that the physics behind the operation of an interferometer based on a Michelson stellar interferometer and the operation of a conventional telescope are almost identical In both cases, it is the second-order correlation function for the field fluctuations over the instrument's aperture that contains the information required to form an image. In the case of the Michelson interferometer, the correlations are carried out point pair by point pair and then

Manuscript approved April 2, 1991

numerically Fourier transformed to give an image. In the case of a telescope, the imaging lens Fourier transforms the field correlation function for all point pairs in the aperture plane and produces an image intensity proportional to this transform. In both cases, the image is formed from the aperture field correlations by Fourier transformation. Only the method for carrying out this transformation is different in the two cases.

2. BASIC IMAGING THEORY

Consider a source of thermal electromagnetic radiation, such as the plume of a booster rocket, that we want to image in some manner. Let the origin of coordinates be located near the center of the source as shown in Fig. 1. The detectors for the imaging device are located over some region of a spherical surface of radius R from the origin.

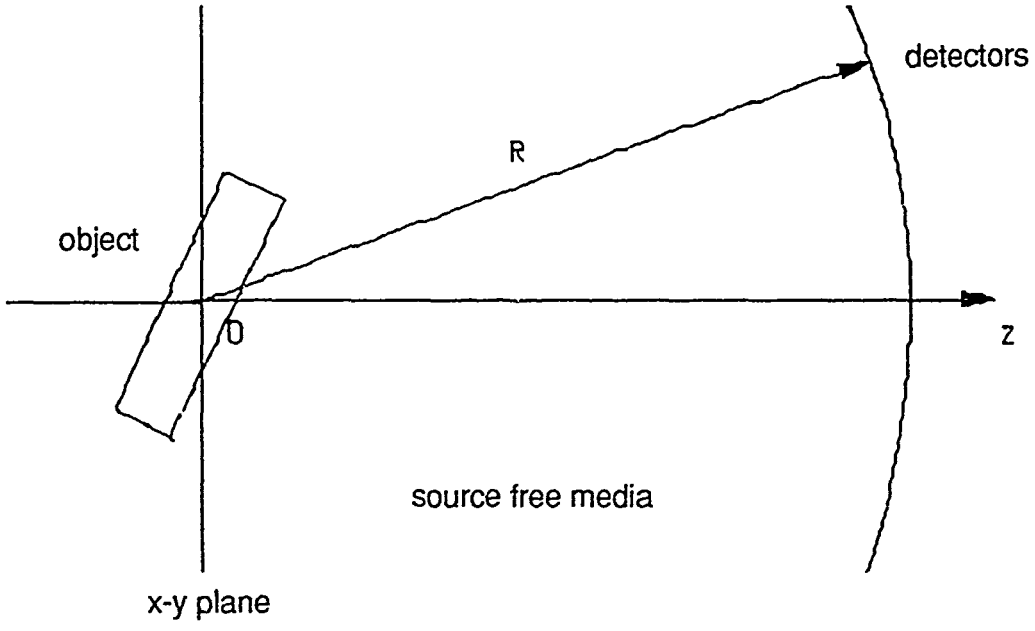

Fig. 1 — The geometry used for the calculations

We assume that the entire, infinite space in Fig. 1 is source free except for the object that we want to image. We further assume that the object is much hotter than its surround so that it radiates a thermal electromagnetic field such that any monochromatic, scalar Cartesian component of the vector field satisfies the inhomogeneous Helmholtz equation [2, Eq. (6.54)]

$$(\nabla^2 + (2\pi)^2)U(\vec{x}) = -4\pi\rho(\vec{x}), \tag{1}$$

where $\rho(\vec{x}')$ is the source distribution within the object, and we express all spatial coordinates in units of one wavelength of the monochromatic field component. The well known Green's function solution to Eq. (1) over an infinite region devoid of any other sources is

$$U(\vec{x}) = \iiint_{\text{source volume}} \rho(\vec{x}')\, e^{2\pi i|\vec{x}-\vec{x}'|}/|\vec{x}-\vec{x}'|\, d^3\vec{x}', \tag{2}$$

[2, Eq. (9.3)], where the primed coordinates represent a radius vector from the origin to a point in the source, and the unprimed coordinates represent a radius vector from the origin to a field point within the half space to the right of the x-y plane in Fig. 1.

If the object can be contained completely within a sphere of radius a, then for any field point $\vec{x}$ outside of the Rayleigh range of the source, we can approximate the Green's function in Eq. (2) by the expansion [2, Eq. (9.7)]

$$e^{2\pi i|\vec{x}-\vec{x}'|}/|\vec{x}-\vec{x}'| \underset{|\vec{x}|>>2\pi a^2}{\approx} [e^{2\pi i|\vec{x}|}/|\vec{x}|]\, e^{-2\pi i\, \vec{x}\cdot\vec{x}'/R}. \tag{3}$$

Thus, if the detector surface is well outside of the Rayleigh range of the source, we can represent the field there by

$$U^{(\infty)}(\vec{x}) = \iiint_{\text{source volume}} \rho(\vec{x}')\, e^{-2\pi i\vec{x}\cdot\vec{x}'/R} d^3\vec{x}'\, e^{2\pi iR}/R, \tag{4}$$

where $R = |\vec{x}|$.

We assume that the intensity of the radiation field is measured by an array of detectors distributed over a portion of a sphere of radius R from the origin in the far field of the source. We further assume that the detectors are sensitive only within the infrared or optical range of wavelengths and that, unlike typical radio receivers, they average over many coherence lengths of the thermal radiation. We also assume that the field is ergodic so that the time-averaged field intensity can be treated by using ensemble averages as is usually done in coherence theory [3]. Then the detectors produce an electric signal proportional to the optical intensity

$$I^{(\infty)}(\vec{x}) = \left\langle U^{(\infty)}(\vec{x})[U^{(\infty)}(\vec{x})]^* \right\rangle, \tag{5}$$

where the sharp brackets denote an ensemble average. To study the propagation of the field from source to detector, we introduce the cross-spectral density function

$$W(\vec{x}_1, \vec{x}_2) = \langle U(\vec{x}_1)\, [U(\vec{x}_2)]^* \rangle, \tag{6}$$

the trace of which is equal to the intensity. Upon substitution from Eq. (4) into Eq. (6), we get

$$W^{(\infty)}(\vec{x}_1, \vec{x}_2) = \iiint_{\text{source volume}} \iiint_{\text{source volume}} W_\rho(\vec{x}_1', \vec{x}_2') \times e^{-2\pi i(\vec{x}_1 \cdot \vec{x}_1' - \vec{x}_2 \cdot \vec{x}_2')/R} d^3\vec{x}_1'\, d^3\vec{x}_2' / R^2, \tag{7}$$

where we define the source correlation function by

$$W_\rho(\vec{x}_1, \vec{x}_2) = \langle \rho(\vec{x}_1)\, \rho^*(\vec{x}_2) \rangle. \tag{8}$$

For the thermal source, we can assume that the source distribution is quasi-homogeneous so that [1]

$$W_\rho(\vec{x}_1', \vec{x}_2') = I_\rho[(\vec{x}_1' + \vec{x}_2')/2]\, \mu_\rho(\vec{x}_1' - \vec{x}_2'), \tag{9}$$

where $I_\rho(\vec{x}_+')$, $\mu_\rho(\vec{x}_-')$ are the intensity and complex degree of spectral coherence over the three-dimensional source, respectively. For a thermal source, it has been shown [4] that

$$\mu_\rho(\vec{x}_-') = \sin(2\pi|\vec{x}_-'|)/(2\pi|\vec{x}_-'|), \tag{10}$$

in units of one wavelength.

By substitution from Eq. (9) into Eq. (7), we get [5,6]

$$W^{(\infty)}(R\vec{s}_1, R\vec{s}_2) = \tilde{I}_\rho(\vec{s}_-)\, \tilde{\mu}_\rho(\vec{s}_+)/R^2, \tag{11}$$

for the cross-spectral density function over the detector array, where

$$\tilde{I}_\rho(\vec{s}_-) = \iiint_{\text{source volume}} I_\rho(\vec{x}_+')\, e^{-2\pi i \vec{x}_+' \cdot \vec{s}_-} d^3\vec{x}_+', \tag{12(a)}$$

and

$$\tilde{\mu}_\rho(\vec{s}_+) = \iiint_{\text{source volume}} \mu_\rho(\vec{x}'_-)\, e^{-2\pi i \vec{x}'_- \cdot \vec{s}_+}\, d^3\vec{x}'_- \tag{12(b))}$$

and where

$$\begin{aligned} \vec{s}_+ &= (\vec{s}_1 + \vec{s}_2)/2, \\ \vec{s}_- &= (\vec{s}_1 - \vec{s}_2), \\ \vec{x}'_+ &= (\vec{x}'_1 + \vec{x}'_2)/2, \\ \vec{x}'_- &= (\vec{x}'_1 - \vec{x}'_2), \end{aligned} \tag{13}$$

in which $\vec{s}_1 = \vec{x}_1 / R$ and $\vec{s}_2 = \vec{x}_2 / R$ are unit vectors from the origin toward the field points $\vec{x}_1$ and $\vec{x}_2$, respectively. Upon substitution from Eq. (10) into Eq. (12(b)), we have

$$\begin{aligned} \tilde{\mu}_\rho(\vec{s}_+) &= \iiint_{\text{source volume}} \sin(2\pi|\vec{x}'_-|)/(2\pi|\vec{x}'_-|)\, e^{-2\pi i \vec{x}'_- \cdot \vec{s}_+}\, d^3\vec{x}'_- \\ &= 4\pi \int_0^\infty \frac{\sin(2\pi r_-)}{2\pi r_-} \frac{\sin(2\pi r_- |\vec{s}_+|)}{2\pi r_- |\vec{s}_+|} r_-^2\, dr_- \\ &= \tfrac{1}{\pi|\vec{s}_+|} \int_0^\infty \sin(2\pi r_-) \sin(2\pi r_- |\vec{s}_+|)\, dr_- \\ &= \frac{\delta(|\vec{s}_+| - 1)}{4\pi|\vec{s}_+|}. \end{aligned} \tag{14}$$

Since $\vec{s}_1$ and $\vec{s}_2$ are unit vectors, it follows from Eq. (13) that $\vec{s}_+$ is also. Thus

$$\tilde{\mu}_\rho(\vec{s}_+) = C \tag{15}$$

is simply a constant proportional to the volume of the object for a thermal source. Upon substitution from Eq. (15) into Eq. (11), we have finally

$$W^{(\infty)}(R\vec{s}_1, R\vec{s}_2) = C\, \tilde{I}_\rho(\vec{s}_1 - \vec{s}_2)/R^2. \tag{16}$$

From Eq.(16), it is clear that the cross-spectral density function is given by components of the three-dimensional Fourier transform of the source intensity. This relationship is much more complicated than it might first appear from Eq.(16). The principle complication arises from the fact

that $W^{(\infty)}(R\vec{s}_1, R\vec{s}_2)$ can be measured only over the surface of the sphere of radius R as shown in Fig. 1, whereas $\tilde{I}_\rho(\vec{s}_1 - \vec{s}_2)$ is a three-dimensional spatial frequency spectrum of the source intensity as shown in Fig. 2. Thus a single measurement of $W^{(\infty)}(R\vec{s}_1, R\vec{s}_2)$ over a portion of the measurement sphere in Fig. 1 only gives data values for $\tilde{I}_\rho(\vec{s}_1 - \vec{s}_2)$ over a portion of a surface within the three-dimensional spatial frequency space of the object intensity distribution $I^{(0)}(\vec{x}'_+)$, as shown in Fig. 2. This is not enough information to perform the three-dimensional Fourier transformation to calculate the image $I^{(0)}(\vec{x}'_+)$. Thus it is easy to calculate $W^{(\infty)}(R\vec{s}_1, R\vec{s}_2)$ given $\tilde{I}_\rho(\vec{s}_1 - \vec{s}_2)$ but not so straightforward to do the inverse, which is what we need to do.

It is the job of our imaging system to measure the cross-spectral density function $W^{(\infty)}(R\vec{s}_1, R\vec{s}_2)$ over the detector plane and to use this information to find $I_\rho(\vec{x}'_+)$. There are two classes of imaging systems that can do this, interferometers and telescopes. In the following sections, we describe both types of systems by using a unified theoretical approach to aid comparisons.

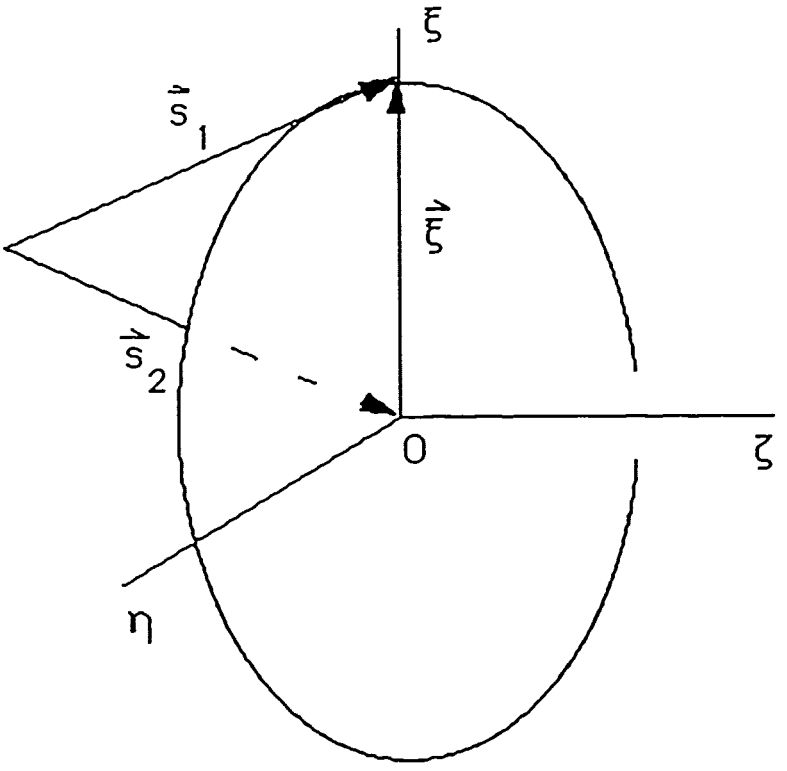

Fig. 2 — Spatial frequency domain of $\tilde{I}_\rho(\vec{s}_1 - \vec{s}_2)$

3. GENERALIZED IMAGING SYSTEM

Almost any linear imaging system can be realized by the generalized imaging system shown in Fig. 3.

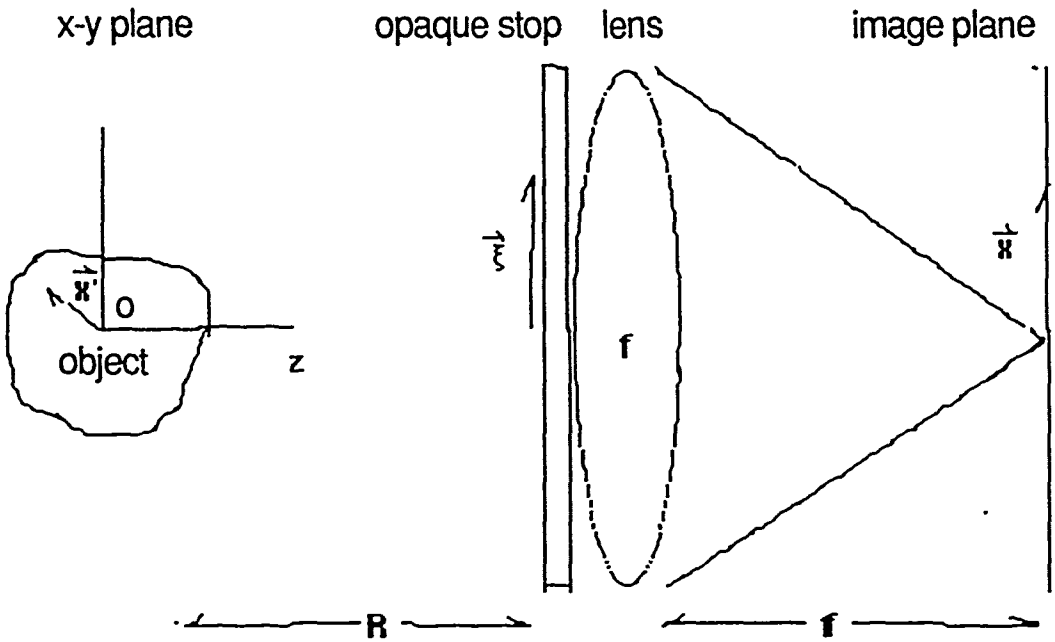

Fig. 3 — Generalized imaging system

This is not a design that is necessarily recommended for actual deployment, but it is extremely useful for comparing the various capabilities of optical imaging systems since this system can mimic almost any known stationary imaging system by the proper choice of holes in the opaque stop. Notice from Fig. 3 that the object, which is assumed to satisfy all of the assumptions made in the last section, radiates a distance R to the imaging system, which is assumed to be outside of the Rayleigh range of the object so that Eq. (16) holds. The imaging system consists simply of an opaque stop pierced with holes that occupies a portion of the detector plane in Fig. 1, a diffraction-limited lens, and an image plane a focal length f away from the lens over which the intensity is measured in some manner. If needed to simulate a more complicated optical system than we will address here, the opaque stop can be replaced by a filter with a complex transmittance function T. Then, as we will show, this generalized imaging system can mimic any linear, spatially stationary two-dimensional system.

As shown in Fig. 3, points within the object are indicated by the radius vector $\vec{x}'$ from the origin; points within the plane of the stop are indicated by the radius vector $\vec{\xi}$ from the z axis within the detector plane; and points within the image plane are indicated by the radius vector $\vec{x}$ from the z axis within the image plane.

Equation (16) gives us the cross-spectral density function over the detector plane, which contains all the information about the object that is present there. In the coordinates of our generalized imaging system, this equation becomes

$$W^{(\infty)}(\vec{\xi}_1, \vec{\xi}_2) = \frac{c}{R^2} \iiint_{\text{source volume}} I_\rho(\vec{x}'_+)\, e^{-2\pi i \vec{x}'_+ \cdot (\vec{\xi}_1 - \vec{\xi}_2)/R}\, d^3\vec{x}'_+ . \tag{17}$$

The stop is assumed to be represented by a transfer function $T(\vec{\xi})$ such that the field amplitude is modified by the relation

$$U_f^{(\infty)}(\vec{\xi}) = U^{(\infty)}(\vec{\xi})\, T(\vec{\xi}), \tag{18}$$

on passage through the holes in the stop. Upon substitution from Eq. (18) into Eq. (6), we find that the cross-spectral density function is modified by

$$\begin{aligned} W_f^{(\infty)}(\vec{\xi}_1, \vec{\xi}_2) &= \left\langle U_f^{(\infty)}(\vec{\xi}_1)[U_f^{(\infty)}(\vec{\xi}_2)]^* \right\rangle \\ &= \left\langle [U^{(\infty)}(\vec{\xi}_1)\, T(\vec{\xi}_1)][U^{(\infty)}(\vec{\xi}_2)\, T(\vec{\xi}_2)]^* \right\rangle \\ &= W^{(\infty)}(\vec{\xi}_1, \vec{\xi}_2) T(\vec{\xi}_1) T^*(\vec{\xi}_2). \end{aligned} \tag{19}$$

The diffraction limited lens can be assumed to take the Fourier transform of the field transmitted by the stop over the detector plane so that the field amplitude over the image plane is [7, Eq. (5-15)]

$$U_i(\vec{x}) = -\frac{i}{f}\, e^{2\pi i (x^2+y^2)/(2f)} \int_{-\infty}^{\infty}\int_{-\infty}^{\infty} U_f(\vec{\xi})\, e^{-2\pi i (\xi x + \eta y)/f}\, d^2\vec{\xi}. \tag{20}$$

Thus, by substitution from this equation into Eq. (5), we get for the intensity observed over the image plane

$$I_i(\vec{x}) = \langle U_i(\vec{x}) U_i^*(\vec{x}) \rangle$$
$$= \frac{1}{f^2} \int\int\int\int W_f^{(-)}(\vec{\xi}_1, \vec{\xi}_2)\, e^{-2\pi i[(\xi_1-\xi_2)x+(\eta_1-\eta_2)y)]/f}\, d^2\vec{\xi}_1 d^2\vec{\xi}_2. \tag{21}$$

Upon substitution from Eqs. (17) and (19) into Eq. (21), we have

$$I_i(\vec{x}) = \frac{C}{R^2 f^2} \int\int\int\int \iiint_{\text{source volume}} I_\rho(\vec{x}'_+)\, e^{-2\pi i \vec{x}'_+ \cdot (\vec{\xi}_1 - \vec{\xi}_2)/R} d^3\vec{x}'_+$$
$$\times T(\vec{\xi}_1) T^*(\vec{\xi}_2) e^{-2\pi i[(\xi_1-\xi_2)x+(\eta_1-\eta_2)y)]/f}\, d^2\vec{\xi}_1 d^2\vec{\xi}_2. \tag{22}$$

Transforming coordinates by using

$$\vec{\xi}_+ = (\vec{\xi}_1 + \vec{\xi}_2)/2,$$
$$\vec{\xi}_- = (\vec{\xi}_1 - \vec{\xi}_2),$$
$$\vec{\xi}_1 = \vec{\xi}_+ + \vec{\xi}_-/2,$$
$$\vec{\xi}_2 = \vec{\xi}_+ - \vec{\xi}_-/2, \tag{23}$$

we get

$$I_i(\vec{x}) = \frac{C}{R^2 f^2} \int\int\int\int \iiint_{\text{source volume}} I_\rho(\vec{x}'_+)\, e^{-2\pi i \vec{x}'_+ \cdot \vec{\xi}_- / R} d^3\vec{x}'_+$$
$$\times T(\vec{\xi}_+ + \vec{\xi}_-/2) T^*(\vec{\xi}_+ - \vec{\xi}_-/2) e^{-2\pi i[\xi_- x+\eta_- y)]/f}\, d^2\vec{\xi}_- d^2\vec{\xi}_+. \tag{24}$$

Equation (24) can be greatly simplified by introducing the modified Fourier optics operators

$$FT_3[I_\rho(\vec{x}')] = \iiint_{\text{source volume}} I_\rho(\vec{x}')\, e^{-2\pi i \vec{x}' \cdot \vec{\xi}_- / R} d^3\vec{x}', \tag{25}$$

$$FT_2[F(\vec{\xi}_-)] = \int\int F(\vec{\xi}_-)\, e^{-2\pi i(\xi_- x+\eta_- y)/f}\, d^2\vec{\xi}_-, \tag{26}$$

and the incoherent transfer function

$$K(\vec{\xi}_-) = \int_{-\infty}^{\infty}\int_{-\infty}^{\infty} T(\vec{\xi}_+ + \vec{\xi}_-/2)T^*(\vec{\xi}_+ - \vec{\xi}_-/2)\, d^2\vec{\xi}_+$$
$$= T(\vec{\xi}_-) \otimes T^*(\vec{\xi}_-), \tag{27}$$

where the operator $\otimes$ denotes an autocorrelation. Thus, by substitution from Eqs. (25), (26), and (27) into Eq. (24), we get

$$I_i(\vec{x}) = \tfrac{C}{R^2 f^2} FT_2[FT_3[I_\rho(\vec{x}')]K(\vec{\xi}_-)]. \tag{28}$$

Equation (28) looks almost like the mathematical description of a a general linear system except for the mixture of two-dimensional and three-dimensional Fourier transforms. The effects of this must be analyzed in more detail.

4. IMAGING SYSTEMS WITH SMALL NUMERICAL APERTURE

Almost any imaging system that is not very near to its object, like a microscope, has a very small numerical aperture. We can safely assume this is the case for any imaging system we might envision for the purposes of this report. Thus we can assume that all of the holes in the stop in Fig. 3 are contained within a circle of radius b. The transmittance function must then be given by

$$T(\vec{\xi}) = 0, \text{ if } \xi^2 + \eta^2 > b^2 \tag{29}$$

outside of this circle. Since the spatial frequencies for $I_\rho(\vec{x}'_+)$ are given by $\vec{\xi}/R = (\xi/R, \eta/R, \zeta/R)$ according to Eq. (25), the stop will block all spatial frequencies except those for which

$$(\xi/R)^2 + (\eta/R)^2 < (b/R)^2, \text{ where } \zeta = \sqrt{R^2 - \xi^2 - \eta^2}. \tag{30}$$

Figure 4 shows the location of these spatial frequencies. Figure 4 also shows that the domain of available data is a portion of a sphere in spatial frequency space with a radius of unity parallel to the ξ, η plane at the origin and which projects a circle of radius b/R onto the ξ, η plane.

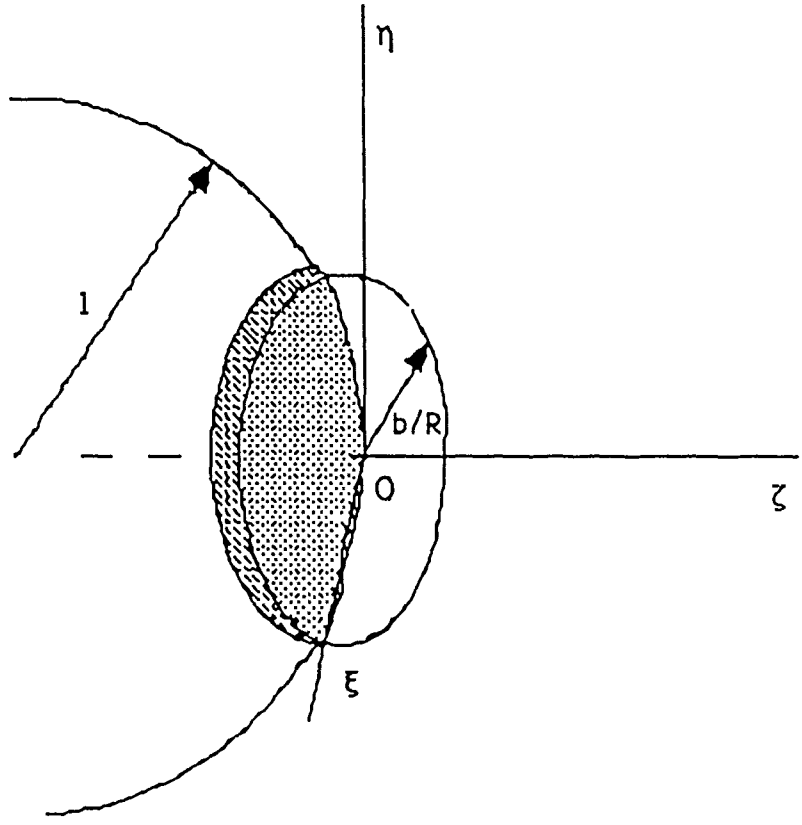

Fig. 4 — Domain of the three-dimensional spatial frequency spectra for the object intensity $I_p(\vec{x}'_+)$. The cross-hatched surface on the sphere illustrates the two-dimensional domain that is available to form an image. The transparent circle is the projection of that data onto the ξ η plane.

Since these spatial frequencies are all that we have, we must study what they can give us rather carefully. To do this most easily, we begin by considering not the complete object intensity $I_\rho(\vec{x}'_+)$ but the projection of it onto the z = 0 plane within the object,

$$
\begin{aligned}
I^{(0)}(x', y', 0) &= \int_{-\infty}^{\infty} I_\rho(\vec{x}')\, dz' \\
&= \int_{-\infty}^{\infty} [\int_{-\infty}^{\infty}\int_{-\infty}^{\infty}\int_{-\infty}^{\infty} \tilde{I}_\rho(\xi/R, \eta/R, \zeta/R)\, e^{2\pi i \vec{x}'\cdot\vec{\xi}/R}\, d^3(\vec{\xi}/R)]\, dz' \\
&= \int_{-\infty}^{\infty}\int_{-\infty}^{\infty}\int_{-\infty}^{\infty} \tilde{I}_\rho(\xi/R, \eta/R, \zeta/R)\, e^{2\pi i(x'\xi + y'\eta)/R} [\int_{-\infty}^{\infty} e^{2\pi i z'\zeta/R}\, dz']\, d^3\vec{\xi}/R \\
&= \int_{-\infty}^{\infty}\int_{-\infty}^{\infty} \tilde{I}_\rho(\xi/R, \eta/R, 0)\, e^{2\pi i(x'\xi + y'\eta)/R}\, d(\xi/R)\, d(\eta/R), \qquad (31)
\end{aligned}
$$

which is the two-dimensional Fourier transform of only the spectral data over the ξ, η plane (in agreement with the well-known projection slice theorem).

From inspection of Fig. 4, we observe that for small enough b, the spectral data that we have available is asymptotically the same as the data over a disk of radius b/R from the origin in the ξ, η plane. Thus, by Fourier inversion of Eq. (31), we have

$$
\tilde{I}_\rho(\xi/R, \eta/R, 0) = \int_{-\infty}^{\infty}\int_{-\infty}^{\infty} I^{(0)}(x', y', 0)\, e^{-2\pi i(x'\xi + y'\eta)/R}\, dx'\, dy', \qquad (32)
$$

an expression for the spatial frequencies over the ξ, η plane. Since this is more than all of the spatial frequencies that are available in an imaging system that has a small numeral aperture, we can replace the three-dimensional Fourier transform in Eq. (28) with Eq. (32) to get

$$
\begin{aligned}
I_i(\vec{x}) = \tfrac{C}{R^2 f^2} \int_{-\infty}^{\infty}\int_{-\infty}^{\infty} [\int_{-\infty}^{\infty}\int_{-\infty}^{\infty} I^{(0)}(x', y', 0)\, e^{-2\pi i(x'\xi_- + y'\eta_-)/R}\, dx'\, dy'] \\
\times K(\vec{\xi}_-)\, e^{-2\pi i[\xi_- x + \eta_- y)]/f}\, d^2\vec{\xi}_-. \qquad (33)
\end{aligned}
$$

Finally, transforming to the unit vector coordinates $\vec{s} = \left(x/f,\, y/f,\, -\sqrt{1-(x/f)^2-(y/f)^2}\right)$ and $\vec{s}' = \left(x'/R,\, y'/R, \sqrt{1-(x'/R)^2+(y'/R)^2}\right)$ from the center of the lens aperture toward the object and image planes, respectively, we have from Eq. (33)

$$I_i(f\vec{s}) = \frac{c}{f^2} FT[FT[I^{(0)}(R\vec{s}')]K(\vec{\xi}_-)], \tag{34}$$

by using the conventional Fourier optics operator

$$FT[F(\vec{\xi})] = \int_{-\infty}^{\infty}\int_{-\infty}^{\infty} F(\vec{\xi})\, e^{-2\pi i(\xi x+\eta y)} d^2\vec{\xi}. \tag{35}$$

Equation (34) is exactly the same as the well known equation describing the data processing by a general linear, stationary two-dimensional system. To simulate such a system with the options shown in Fig. 3, we need only require that the (sometimes complex) $k(\vec{\xi}_-)$ function defined by Eq. (27) can be physically realized. The input data to Eq. (34) is seen not to be the three-dimensional intensity of the object $I_\rho(\vec{x}'_+)$ but rather the projection of this intensity onto the z = 0 plane $I^{(0)}(R\vec{s}')$. Thus all depth information is lost because of the limited data collection area on the detector plane.

A useful property for comparing imaging systems is the image of a point object, called the point-spread function. To derive an expression for the point-spread function, we first apply the famous convolution theorem [7, pg. 10] to Eq. (34) to get

$$I_i(f\vec{s}) = \frac{c}{f^2}\left[\int_{-\infty}^{\infty}\int_{-\infty}^{\infty} K(\vec{\xi}_-)\, e^{-2\pi i(\xi_- s_x+\eta_- s_y)}\, d^2\vec{\xi}_-\right] * I^{(0)}(-R\vec{s}), \tag{36}$$

and then set the projected object intensity function $I^{(0)}(R\vec{s}')$ to a point object, i.e.,

$$I^{(0)}(R\vec{s}') = \delta^2(R\vec{s}'), \tag{37}$$

in Eq. (36). We then substitute from (27), and use the autocorrelation theorem [7, p. 10] to get

$$\begin{aligned} h(\vec{s}) &= \frac{c}{f^2} FT[K(\vec{\xi}_-)] * \delta^2(-R\vec{s}') \\ &= \frac{c}{f^2} FT[K(\vec{\xi}_-)] \\ &= \frac{c}{f^2} FT[T(\vec{\xi}_-) \otimes T^*(\vec{\xi}_-)] \\ &= \frac{c}{f^2} \left|\tilde{T}(\vec{s})\right|^2 \\ &= \frac{c}{f^2} \left| \int_{-\infty}^{\infty} \int_{-\infty}^{\infty} T(\vec{\xi}_-)\, e^{2\pi i(\xi_- s_x + \eta_- s_y)}\, d^2\vec{\xi}_- \right|^2 . \end{aligned} \tag{38}$$

Equation (38) gives the point spread function for our generalized imaging system when illuminated by a quasi-homogeneous source. Clearly it is a function of only $T(\vec{\xi}_-)$, the transmittance function of the stop. By substituting from the second line of Eq. (38) into Eq. (36), we have the very important equation

$$I_i(f\vec{s}) = h(\vec{s}) * I^{(0)}(-R\vec{s}). \tag{39}$$

From this equation we see the importance of the spread function for analyzing imaging systems. The image is just the object function convolved with the spread function. If the spread function were a Dirac delta function at the origin, the image would be a perfect replica of the object. Since this never happens, what we want is a system that has as sharp a peak as possible at the origin and is as close to zero as possible everywhere else to minimize background noise to the image. We will look for such systems.

We have developed the generalized system as much as possible without making assumptions that limit its application. In the following sections, we will use this system to analyze the imaging properties of several interferometers and telescopes that might be used as sensors for detecting and identifying the target of interest.

5. INTERFEROMETERS

An optical interferometer is not really so different from an ordinary telescope within this theory, although the manner in which the instrument is actually realized can be very much different. To simulate the operation of an interferometer, we use a stop (in the position shown in

Fig. 3) that has small pinholes in it. The very simplest such stop would have a single pinhole on the optic axis so that its transmittance function is given by

$$T(\vec{\xi}) = \delta^2(\vec{\xi}). \tag{40}$$

With this aperture, the generalized imaging system would behave as a pinhole camera, the lens having no effect on the light from a single point other than a simple phase shift. This case is actually very difficult to treat since it requires a geometrical optics limit to the diffraction theory used here [8]. To do this requires that we set up the diffraction integrals represented by Eq. (34), and then evaluate them in a special way by using the method of stationary phase. Since such an imaging device isn't presently considered very practical (very little light is admitted through one pinhole) and the analysis is very long and complicated, we will not pursue this case further.

The next case is with a stop having two symmetrically placed pinholes (about the origin) a distance d apart so that the transmittance function becomes

$$T(\vec{\xi}) = \delta(\xi - d/2)\,\delta(\eta) + \delta(\xi + d/2)\,\delta(\eta). \tag{41}$$

This turns out to be a very important case for the purposes of this study. This is an analog to the Michelson stellar interferometer [9 , p. 275] and also the radio interferometer used as an element of a radio telescope. For a radio telescope, the interferometer does not have the physical form of our generalized imaging system with a transmittance function given by Eq. (40). It would not be practical to build a radio frequency lens the size of the Earth's orbit about the Sun (the values of d can sometimes be that large in radio astronomy), but the basic mathematical models for a single element of a radio telescope and our device are the same. Upon substitution from Eq. (41) into Eq. (38), we get

$$h(\vec{s}) = \frac{c}{f^2}\,[2 + 2\cos(2\pi d s_x)], \tag{42}$$

where

$$K(\vec{\xi}) = \delta(\xi - d)\,\delta(\eta) + 2\,\delta(\xi)\delta(\eta) + \delta(\xi + d)\delta(\eta). \tag{43}$$

This is the point-spread function for the Michelson stellar interferometer. Figure 5 shows a simulation of this spread function obtained with the computer program Mathematica.

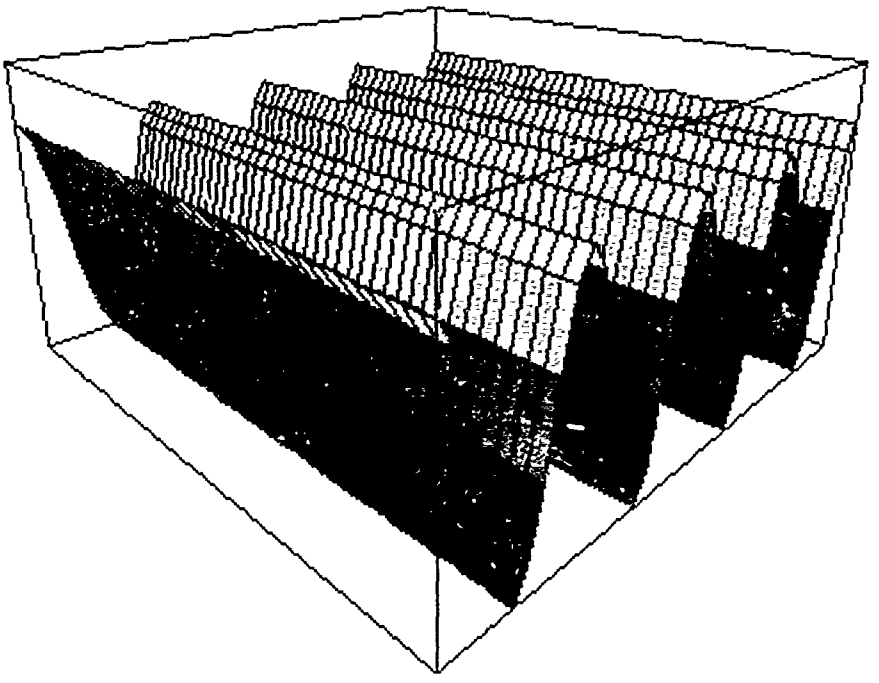

Fig. 5 — Mathematica simulation of the point-spread function for a Michelson interferometer as given analytically by Eq. (41)

We note from Fig. 5 that the Michelson interferometer does not have a spread function that has a sharp, single peak at the origin. Thus when this spread function is convolved with the object function, it cannot produce an image. From Eq. (43), it is clear that this interferometer gives only one spatial frequency component of the image so that for a point object (which contains all frequency components with equal magnitude), the image is the single spatial frequency shown in Fig. 5. This interferometer is used in radio astronomy because for radio waves, we are limited to a very few point detectors (radio receivers) that are each very expensive (generally with very large parabolic dish antennas). Thus the Michelson interferometer is mandated by physical constraints as well as history. A radio telescope is made up of many Michelson interferometers each giving the magnitude and phase of only one spatial frequency component of the required image. Spatial frequency data are collected from many such interferometers until enough are available to do an approximate inverse Fourier transform to obtain the image. This method can be applied to imaging sources of quasi-homogeneous light as well as radio waves. There are some obvious advantages to such an approach. The small area required to collect light for each of the two pinholes makes for two, very light-weight, compact collectors. Images can be produced, of course, only if the light received by the two collectors can be made to interfere; and also, if a common phase reference can be maintained for the complex data from all of the interferometers. Some disadvantages of imaging

with interferometers are the low sensitivity due to the small amount of light available to each collector and the long time required to obtain enough spatial frequency data and process it to form the image.

The next, more complicated interferometer would have three pinholes arranged at the corners of an equilateral triangle with sides of length d. The transmittance function would then become

$$T(\bar{\xi}) = \delta(\xi)\delta(\eta - d/\sqrt{3}) + \delta(\xi - 2d/\sqrt{3})\delta(\eta + d/\sqrt{3}) + \delta(\xi + 2d/\sqrt{3})\delta(\eta + d/\sqrt{3}). \quad (44)$$

By substitution from Eq. (44) into Eq. (38) and evaluating the result numerically, we get the point-spread function illustrated in Fig. 6.

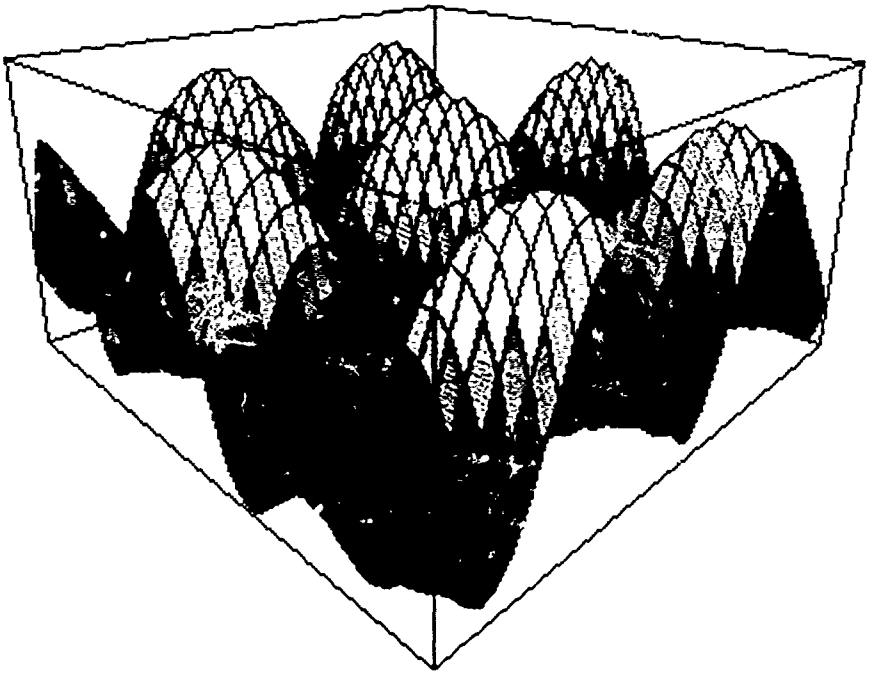

Fig. 6 — Mathematica simulation of the point-spread function for an interferometer with a three-point aperture as given by Eq. (44)

This interferometer gives us an image by using six spatial frequency components from the object, which are equally weighted, plus a more heavily weighted DC component. From Fig. 6, it is clear that there is no single, central maximum at the origin. Thus we still can't get an image

from only one such interferometer. To my knowledge, no work has been done on the use of an array of such interferometers to form an image by the sort of aperture synthesis used in radio interferometer. Isolating the six spatial frequencies from each interferometer might be a problem.

The next, more complicated interferometer would have four pinholes located at the corners of a square box so that the transmittance function would become

$$\begin{aligned} T(\vec{\xi}) = {} & \delta(\xi - d)\,\delta(\eta - d) \\ & + \delta(\xi - d)\delta(\eta + d) \\ & + \delta(\xi + d)\delta(\eta - d) \\ & + \delta(\xi + d)\delta(\eta + d). \end{aligned} \tag{45}$$

Upon substitution from Eq. (45) into Eq. (38) and again by using numerical evaluation, we get the point-spread function illustrated in Fig. 7.

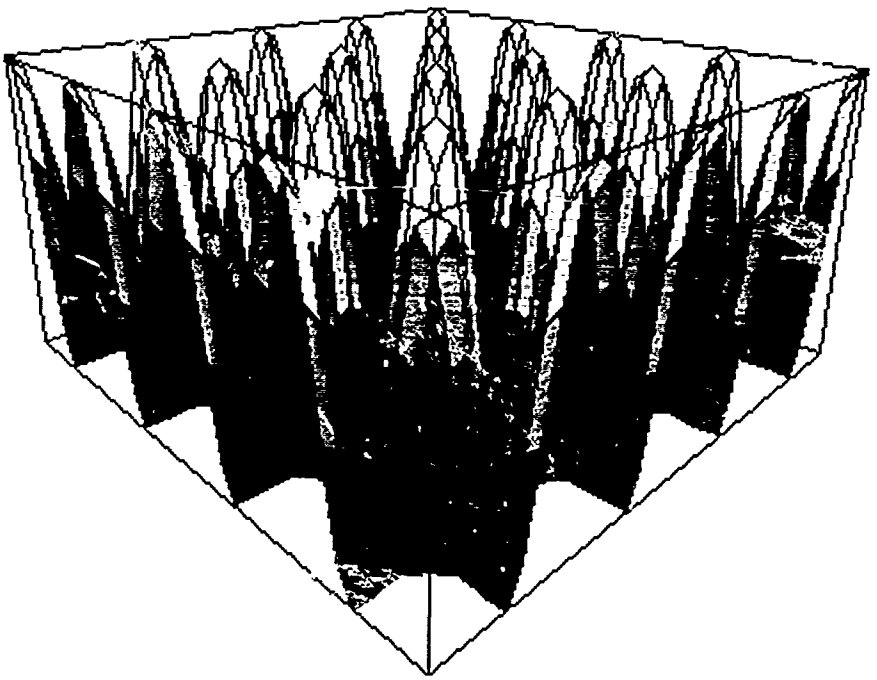

Fig. 7 — Mathematica simulation of the point-spread function for an interferometer with a four-point aperture as given by Eq. (45)

For the four-pinhole interferometer, the image is made up of ten spatial frequency components; a DC component weighted 4, four components on the Cartesian axes weighted 2, and four on the diagonals weighted 1. Since Fig. 7 shows no single maximum at the origin, this interferometer also gives no image if used alone.

We will define an interferometer (as opposed to a telescope) as an optical system like those described so far that do not form images. This is not to say that data from an array of such interferometers cannot be used to form an image, as is the case for the Michelson interferometer used in radio astronomy. This definition applies to a single interferometer. If we increase the number of pinholes enough with a center of symmetry at the center of them, we eventually find that the spread function has a large maxima at the origin so that a true image forms when the spread function is convolved with the object function. Such systems will be called telescopes and are the subject of the next section.

6. TELESCOPES

A telescope is simply an interferometer that has a sufficient number of pinholes in its aperture, symmetrically arranged, such that its point-spread function has a strong peak at the origin.

The first telescope that we will consider has a "wye" aperture with a transmittance function given by

$$\begin{aligned} T(\bar{\xi}) = {} & \delta(\xi)\, step(\eta) \\ & + step(-\eta)\, \delta(\xi - \eta/2) \\ & + step(-\eta)\, \delta(\xi + \eta/2), \text{ if } \xi^2 + \eta^2 \le d^2, \\ = {} & 0, \text{ otherwise.} \end{aligned} \tag{46}$$

This instrument is a simple extension of the three-hole interferometer described above that has a continuous distribution of pinholes added along the lines in the directions from the origins to the three original pinholes. When observed in the x-y plane, this aperture forms an upside-down letter wye. Upon substitution from Eq. (46) into Eq. (38), we obtain the spread function shown in Fig. 8. From this figure, we notice that the addition of the extra pinholes has produced a strong peak at the origin. Thus the image formed by convolution of the object function with the spread function shown in Fig. 8 (as described by Eq. (39)) is a recognizable replica of the object. The resolution is limited by the diameter of the central peak in Fig. 8, and the background noise is limited by the rather significant side lobes. This is the price that we pay for the limited number of pinholes in the

aperture. But, at the same time, we gain the advantage of a very lightweight system since light need only be collected along three one-dimensional collector arrays.

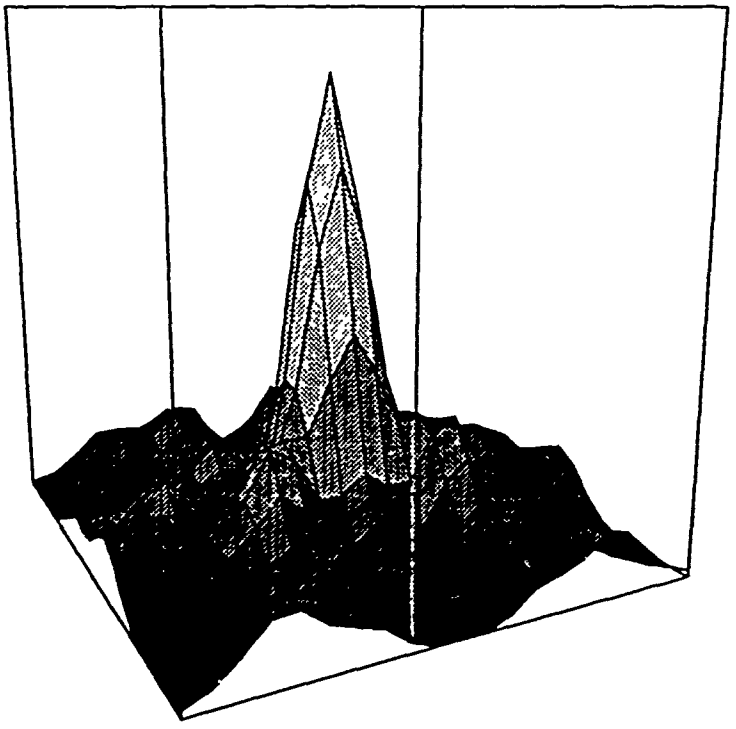

Fig. 8 — Mathematica simulation of the point-spread function for a wye aperture as given by Eq. (46)

A system with better resolution and noise can be realized without much additional weight by a telescope with a narrow, annular aperture with the transmittance function given by

$$T(\vec{\xi}) = \delta(\sqrt{\xi^2 + \eta^2} - d) / d. \tag{47}$$

By substitution from Eq. (47) into Eq. (38), we obtain the spread function shown in Fig. 9. Comparison of Figs. 8 and 9 make the improvement in noise apparent.

The best, general-purpose telescope is, of course, the filled, circular aperture that has been conventional since Galileo's time. This instrument has a transfer function given by

$$T(\vec{\xi}) = circ(\sqrt{\xi^2 + \eta^2} / d). \tag{48}$$

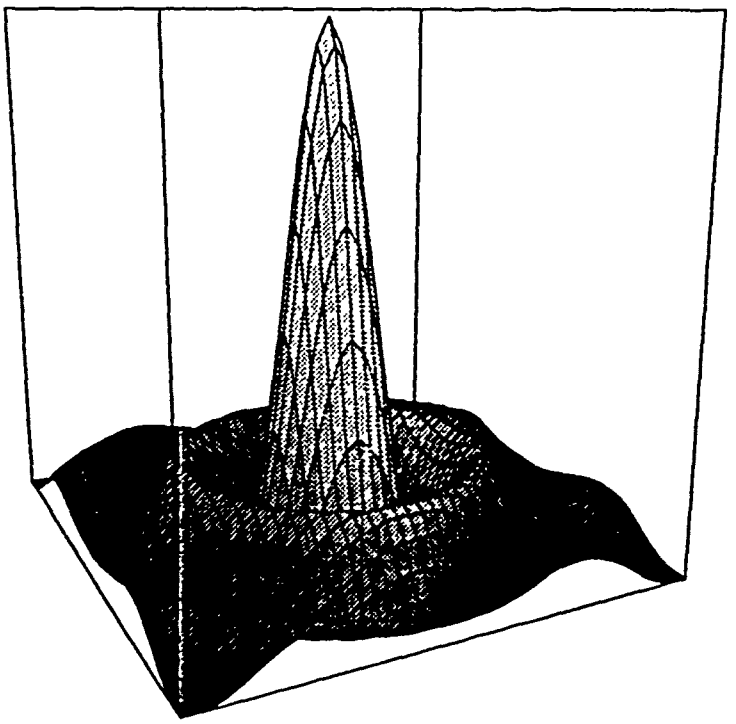

Fig. 9 — Mathematica simulation of the point-spread function for a thin, annular aperture as given by Eq. (47)

By substituting from Eq. (48) into Eq. (38), we get the famous Airy disk pattern

$$h(\vec{s}) = \frac{c}{f^2}\,[2J_1(\pi dx)/(\pi dx)]^2, \tag{49}$$

which is illustrated in Fig. 10. The smallest interval in the object that can be resolved in the image after convolution of the object function with this spread function is given by the well-known expression

$$\delta = 0.61\ f/d, \tag{50}$$

in spatial units of one wavelength, which is easily calculated from the width of the central lobe in Eq. (49) [9, Eq. (8.6.3.32)]. By comparison of Fig. 10 with Figs. 6 through 9, we readily see that this is, far and away, the best spread function. It has the lowest side lobes. Thus it gives the least noise. It also, however, requires the largest aperture. For a refractive system, the weight of the lens alone rapidly becomes impractical as d is increased to improve the resolution as given by Eq. (50). For a reflective system, the primary mirror is much lighter than a lens, but still gets heavier and heavier as d is increased. Thus, a trade-off must be sought between weight and the

added noise effects and loss of light from a sparse aperture. These are very practical engineering problems involving detailed design and materials technology well beyond the scope of this tutorial treatment of basic imaging theory; however, the theory developed here might be of some use in the design.

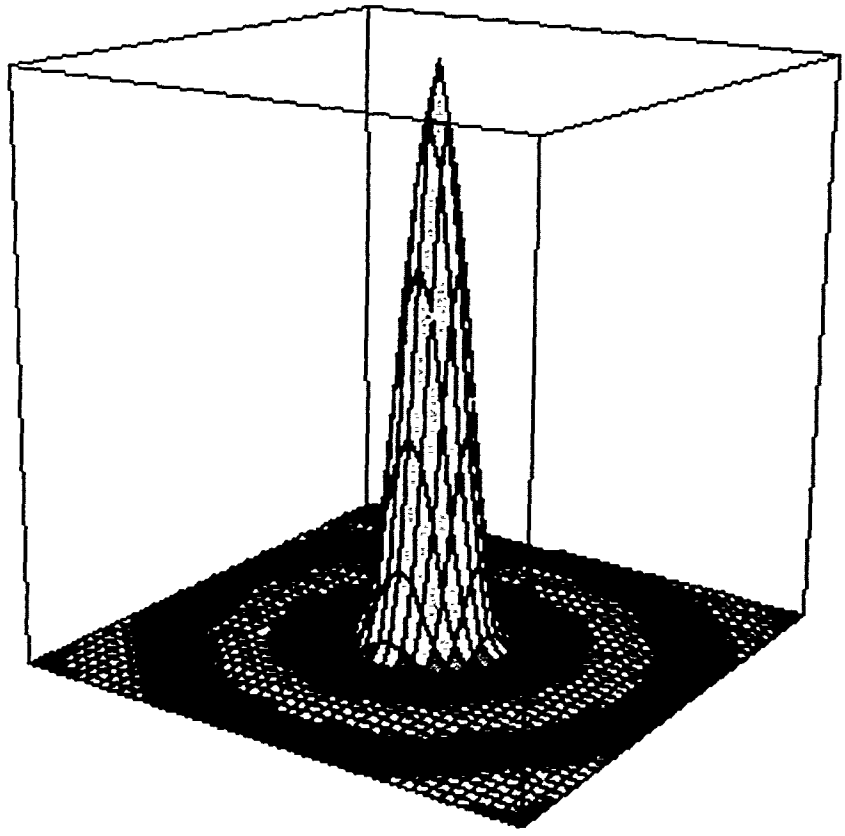

Fig. 10 — Mathematica simulation of the point-spread function for a circular aperture as given by Eq. (48)

7. CONCLUSIONS

We see easily from this analysis that the method for forming the image by using an interferometer and a telescope are identical from a purely theoretical standpoint, as based on the model developed in this report. In both cases, it is the cross-spectral density function in the aperture plane of the instrument that carries the necessary information to obtain an image.

In the case of the Michelson stellar interferometer, the complex degree of spectral coherence is measured specifically by using interference patterns as illustrated in Fig. 5. From the measurement of the relative modulation depth and phase shift of the illustrated sinusoidal pattern at the origin in this figure, the amplitude and phase for the cross-spectral density function for points in the aperture separated by d, the distance between the pinholes in Eq. (41) can be determined. Such data are collected for all possible values of d within the aperture of the instrument, and these data are then Fourier transformed into an image of the object as described by Carter [10, Eq. (5.1)]. This is the way that a radio telescope is operated.

For an ordinary telescope, the imaging lens systems performs exactly the same operations as described above for the radio telescope. The lens performs a Fourier transformation on the cross-spectral density function over the aperture plane as given by Eq. (21), which yields the image over the image plane.

Clearly, from the point of view of this model, the systems are identical. They only differ physically in the manner in which the Fourier transform of the cross-spectral density function over the aperture plane is taken. One would expect similar image quality from either approach to imaging so long as the available data from the aperture plane are the same. Some differences would arise, of course, because of the very different physical limitations of the two systems to detect the cross-spectral density function precisely and perform the required Fourier transform. Comparisons of the image quality for a telescope and an interferometer based on an analysis of the actual physical limitations for the two systems would require detailed systems designs and is beyond the scope of this theoretical analysis.

Information concerning the detection and location of the booster rocket might be obtained from a very limited number of interferometers by using point-spread function patterns of the type illustrated in Figs. 5, 6, and 7. This might be an interesting approach for study since it might achieve the goals of the "Brilliant Eyes" system with less size and weight than that required for a conventional telescope.

8. REFERENCES

1. W. H. Carter and E. Wolf, "Coherence and Radiometry with Quasihomogeneous Planar Sources," *J. Opt. Soc. Am.* 67, 785-796 (1977).

2. J. D. Jackson, *Classical Electrodynamics* (Wiley, New York, 1962).

3. J. Perina, *Coherence of Light* (Reidel, Boston, 1985).

4. J. T. Foley, W. H. Carter, and E. Wolf, "Field Correlations within a Completely Incoherent Primary Spherical Source," *J. Opt. Soc. Am.* **3A**, 1090-1096 (1986).

5. W. H. Carter and E. Wolf, "Correlation Theory of Wavefields Generated by Fluctuating Three-dimensional, Primary, Scalar Sources: I. General Theory," *Optica Acta* **28**, 227-244 (1981).

6. W. H. Carter and E. Wolf, "Correlation Theory of Wavefields Generated by Fluctuating Three-dimensional, Primary, Scalar Sources: II. Radiation from Isotropic Model Sources," *Optica Acta* **28**, 245-259 (1981).

7. J. W. Goodman, *Introduction to Fourier Optics* (McGraw-Hill, New York, 1968).

8. R. E. Swing, "General Transfer Function for the Pinhole Camera," *J. Opt. Soc. Am.* **58**, 629-635 (1968).

9. M. Born and E. Wolf, *Principles of Optics* (Pergamon Press, New York, 1975).

10. W. H. Carter, "Three Different kinds of Fraunhofer Approximations. II. Propagation of the Cross-spectral Density Function," *J. Mod. Opt.* **37**, 109-120 (1990).